Soft Matter

ROYAL SOCIETY OF CHEMISTRY

PAPER

View Article Online
View Journal | View Issue

Cite this: *Soft Matter*, 2022, **18**, 9076

Modelling the compression of a soft ellipsoid fingertip

Ge Shi, Azadeh Shariati, Ian Eames and Helge Wurdemann *

A purely mechanical-driven haptic feedback system was developed for amputees by [G. Shi *et al.*, *IEEE Trans. Haptics*, 2020, **13**, 204–210]. The fingertip ellipsoid modulates the compression force and transmits it to the feedback actuator when the finger interacts with an object. In this paper, the haptic feedback system has been modelled using finite deformation theory. For the ellipsoid fingertip, the compression behaviour between two rigid, flat surfaces has been studied and can predict the force-indentation trend and deformed shape of the membrane with the contact area. For the feedback actuator, the model for the flat membrane is developed with elastic theory, in which the deformation resulting in contact area increase has been studied. The model has been validated with experimental results, which consists of the fingertip ellipsoid membrane being compressed by a rigid surface and the feedback actuator being pressurised. The results of force-indentation, pressure-indentation and the deformation of the membrane from ellipsoid modelling lay within the experimental data and fit the non-linear trend well. The results from modelling the feedback actuator have the same trend as the experimental data in the force–pressure relationship. The haptic feedback system is consistent as a functional tactile sensor after validation. We present the modelling and validation of the proposed model for the mechanical driven haptic feedback system.

Received 8th June 2022,
Accepted 31st October 2022

DOI: 10.1039/d2sm00763k

rsc.li/soft-matter-journal

1 Introduction

Existing prosthetic devices for amputees with upper-limb amputation range from cosmetic prostheses to body-powered and highly dexterous myo-electronic hand prosthetic devices. Extensive advancements have been achieved in providing amputees with sensation through (non-)invasive haptic feedback systems.

Although research from ref. 1 and 2 provide reviews of mechano, vibro, electrotactile and hybrid systems, purely mechanical-driven feedback approaches, however, are seldom investigated. In 1933, Rosset described how pressure at the prosthetic fingertip could be transmitted to amputees.[3] In 1953, Conzelman *et al.* were granted a patent on a similar haptic feedback system with incompressible fluid.[4] In ref. 5, this initial idea resulted in a pneumatic closed-loop haptic feedback system prototype, which used compressible air instead of incompressible fluid, and was validated by subjects. Technical challenges of the two aforementioned approaches include the liability (*i.e.*, appearance of leakages) and fabrication process. Pneumatic transmission has further limitations due to its density and compressibility when displacement of only a few millilitres in volume is required. In ref. 6, hydraulic haptic feedback system with conductive fluid and electronics to actuate was introduced and validated. The related PCBs and battery squeezed into upper-limb prosthetic give the amputees extra weight to carry. In ref. 7, we presented the development and evaluation of a 3D printed mechano-tactile haptic feedback system using a soft hydraulic tactile fingertip sensor. This haptic feedback system is purely mechanical and relies on a coupled hydraulic system. The latest technology in multi-material additive manufacturing, such as the Stratasys Objet500 Connex3, allows printing of dual material such as VeroClear, a polymethyl methacrylate, and Agilus 30, a thermoplastic elastomer with flexible, rubber-like qualities. Our haptic feedback system is made of an Agilus 30 fingertip sensor integrated with a VeroClear finger linked to a wearable haptic mechano-tactile actuator with an Agilus 30 membrane. The sensor and actuator are 3D printed and can be easily integrated into (3D printed) body-powered upper-limb prostheses. In the case of distal amputations, such as transradial amputees, the haptic feedback actuator can be interfaced with the residual limb/forearm through a socket. The range of forces that can be transmitted using our haptic feedback interface relies on the dimension of the design of the fingertip and haptic feedback actuator as well as the used material.

In this paper, we propose an analytical modelling approach for a fluidic haptic feedback system by understanding the deformation of the ellipsoid soft membrane (resulting in fluidic

Department of Mechanical Engineering, University College London, London, UK. E-mail: h.wurdemann@ucl.ac.uk

pressure change) and then the transmission of pressure to the haptic feedback membrane resulting in tactile forces. On the other hand, our analytical model will be able to provide the basis for future optimisation problems for the design for sensing interfaces based on ellipsoid membranes, for instance. In this sense, the design of membranes could be optimised by considering a defined force range as input and understanding, what material and geometric dimensions a sensor should be made of.

Despite the application of our proposed model to the fluidic haptic feedback system in this paper, there are a number of soft robotic areas that might benefit from our mathematical formulation. In general, our approach might support kinematic modelling of robotic structures that are made of a number of soft elastic membranes. Input such as the dimension of the membrane, material properties and membrane thickness will then return the overall deformation and compression of each. In particular, examples might include the locomotion of a bio-inspired robot made of a series of silicone elastomer spheres that are deformed by shape memory allow coils[8] or a robotic manipulator made of stackable Hyperelastic Ballooning Membranes.[9] Our analytical model would be able to determine the deformed shape of the membranes under certain forces and, hence, the motion of the actuators. Other examples concern the creation of tactile sensing elements that are pre-shaped ellipsoid membranes.[10–13] Here, our mathematical model would be suitable to establish a calibration curve between the compression and the force acting on the membranes. For instance, the BioTac SP tactile sensor by Syntouch is made of an ellipsoid membrane which is filled with incompressible fluid inside the cavity able to measure mechano- and vibro-tactile forces through the pressure change. With our proposed analytical model, any deformation would return an increase in hydrostatic pressure and result in a force response. Beyond the application in the field of soft material robotics, ellipsoid membranes further exist in biological cells (fat cells and liver hepatocytes), tumours and organs (glands), which our analytical model could be applied to.[14–16] Examples include studies on mechanical properties of capsules and biological cells with ellipsoid shapes.[17–19] Applying our analytical model could help to diagnose unhealthy soft tissue and distinguish cancerous from healthy tissue during palpation and compression procedures.[20]

2 Background on modelling deformation of elastic pockets

The compression of an elastic membrane pocket by a rigid surface was first proposed by Mooney and Rivlin in 1940 and 1948.[21,22] They established a theory of large deformations of elastic membrane pockets, which applies the hyper-elastic model to describe the relationship between deformation and stored energy. Based on the material theory, Adkins *et al.* solved the problem of thin elastic membrane inflation[23] and proposed an approach based on the conversion of boundary conditions into an initial condition problem for an axisymmetric membrane. Hence, a number of problems have been studied based on the large deformation theory with different geometries, *e.g.*, circular or square elastic membrane inflation was reformulated by simplified governing equations.[24,25] By using the modified governing system of equations, the problem can be solved by a standard analytical method with appropriate boundary conditions, which was extended by Bouremel *et al.* for the free inflation and compression problem.[26]

The problem of inflation and compression with different geometries rather than flat membrane inflation have been investigated in detail. For instance, Feng *et al.* studied the inflation of an axisymmetric semi-spherical elastic membrane that compressed with a flat rigid plate with a rigid support underneath.[27] This model has been widely applied and its feasibility validated through applications such as micro-capsule and cell wall modelling,[18,19,28,29] safety airbag modelling,[30] modelling the behaviour of the membrane in contact with curved surfaces.[31] Inflation and compression of toroidal membranes, in which the geometry has positive and negative curvatures, have also been studied.[32,33] In addition, the inflation and compression of an elliptical membrane as a fingertip pulp model has been modelled by Serina.[34] However, the mismatch of the angle in the parametric equation and polar coordinator causes the model to be less accurate.

In addition to the continuous elastic deformation theory, other methods have been applied to model the fingertip, such as Finite Element Analysis (FEA) and the static elastic model. In ref. 35, fingertip pulp was modelled as a solid elastic semi-sphere composed of an infinite number of vertical springs. In ref. 36 and 37, the compression of a fingertip was modelled by FEA methods and the force response fits the results of the model in ref. 34.

Fingertip modelling in the existing literature either requires tremendous computation like FEA or assumes the fingertip behaves as an elastic chunk and cannot predict the shape of deformation. As a result, the analytical method for calculating the compression of an ellipsoid fingertip membrane is still undeveloped. Hence, the contribution of our paper lies in a new analytical model for an ellipsoid geometry membrane allowing us to understand the change in shape, volume and, hence, pressure during deformation. We distinguish the non-linearity caused both by the ellipsoid shape and hyperelasity of materials. The results of our proposed model have been used to model and experimentally validate the response of the feedback actuator in order to predict the performance of a haptic feedback system with different material, different dimensions.

3 Mathematical model

3.1 Ellipsoid membrane model

The assumptions and conditions of this analysis are:

- The ellipsoid membrane is axisymmetric in both undeformed and deformed conditions, and the shear stresses are zero from the profile view.

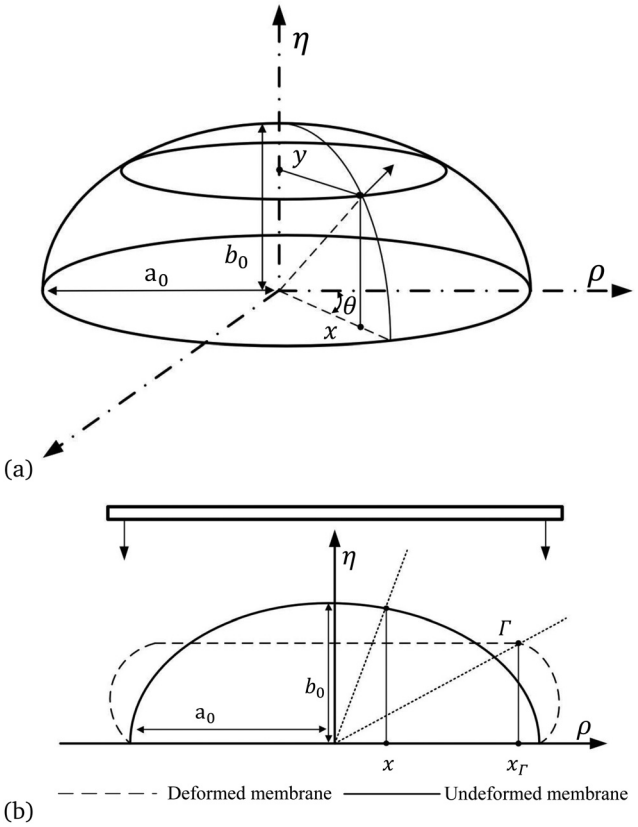

Fig. 1 (a) Overview of the ellipsoid membrane in Cartesian coordinates. (b) Schematic of the axisymmetric membrane model showing the undeformed and compressed configurations. Half of the model and one plate are shown. a_0 and b_0 are the major and minor axes of the ellipsoid, respectively. x_Γ is the boundary position between the contact region and free inflation region.

• The thickness of the ellipsoid membrane h_0 is small relative to the entire dimensions, and therefore the change of thickness during deformation is considered negligible.

• The volume of the ellipsoid membrane is constant during compression due to the fluid being relatively incompressible.

• The pressure under the contact region is evenly distributed and equal to the pressure inside.

The fingertip is assumed as an ellipsoid membrane that is compressed vertically and quasi-statically by a flat, rigid, smooth plate from the top as shown in Fig. 1. The membrane is modelled as an axisymmetric, ellipsoid membrane with rigid fixed support underneath and filled with incompressible, inviscid fluid. The membrane is fitted into the cylindrical coordinates (x,y,θ) to describe the shape in its undeformed state. The centroid of the ellipsoid membrane is located at the origin with a major principal axis length a_0 on the x axis and the minor principal axis length b_0 on the y axis. The second cylindrical coordinates (ρ,η,θ) are used for compressed ellipsoid membranes. The x_Γ denotes the value of x corresponding to the boundary Γ between the contact and free inflation regions. Elastic materials that can be fitted by a hyperelastic model, *e.g.*, the Mooney–Rivlin model, Yeoh, or neo-Hookean model, are compatible with our model. In general, compatible materials would need to satisfy a number of criteria such as: it can be assumed that the material is incompressible, capable of large deformations and able to return to its initial state.

3.1.1 Potential energy function. The incompressible elastic material of the membrane is modelled using the Mooney–Rivlin model and the potential strain-energy density function W is defined by

$$W = C_1(I_1 - 3) + C_2(I_2 - 3), \tag{1}$$

with C_1, C_2 as material constants, and the principal strain invariants I_1 and I_2 related to the principal stretch ratios, λ_1, λ_2 are:

$$\begin{aligned} I_1 &= \lambda_1^2 + \lambda_2^2 + \frac{1}{\lambda_1^2\lambda_2^2}, \\ I_2 &= \frac{1}{\lambda_1^2} + \frac{1}{\lambda_2^2} + \lambda_1^2\lambda_2^2. \end{aligned} \tag{2}$$

3.1.2 Free-inflation region. Along the meridian direction, the infinitesimal arc length of the undeformed membrane is defined as ds, which is located by horizontal position x in the coordinate, and the deformed arc length is dS:

$$\begin{aligned} \mathrm{d}s &= (\mathrm{d}x^2 + \mathrm{d}y^2)^{1/2} = (1 + e(x)^2)^{1/2}\mathrm{d}x, \\ \mathrm{d}S &= (\mathrm{d}\rho^2 + \mathrm{d}\eta^2)^{1/2}, \end{aligned} \tag{3}$$

where $e(x) = \left(\frac{-2b_0x}{a_0\sqrt{a_0^2 - x^2}}\right)^{1/2}$ obtained by ellipse standard equation $\frac{x^2}{a_0^2} + \frac{y^2}{b_0^2} = 1$. Throughout the paper, subscripts 1 and 2 indicate the variates in meridian and circumferential direction, respectively. The prime in the equations denotes the derivatives with respect to horizontal position x.

The principal stretch ratio λ_1 is in meridian direction subscripts 1 and λ_2 is in circumferential direction with subscripts 2, defined as the ratio between the undeformed lengths of an infinitesimal arc element and the deformed lengths, are:

$$\begin{aligned} \lambda_1 &= \frac{\mathrm{d}S}{\mathrm{d}s} = \frac{(\rho'(x)^2 + \eta'(x)^2)^{1/2}}{(1 + e(x)^2)^{1/2}}, \\ \lambda_2 &= \frac{\rho(x)}{x}. \end{aligned} \tag{4}$$

The equilibrium equations for the membrane in both meridian tangential and normal direction are:[27]

$$\begin{aligned} &\frac{\mathrm{d}T_1}{\mathrm{d}\rho} + \frac{1}{\rho}(T_1 - T_2) = 0, \\ &k_1T_1 + k_2T_2 = P, \end{aligned} \tag{5}$$

where P is the hydrostatic pressure inside the ellipsoid membrane. The stress resultants of each membrane segment are given by:

$$T_i = 2h_0\frac{1}{\lambda_1\lambda_2}\left(\lambda_i^2\frac{\partial W}{\partial I_1} - \frac{1}{\lambda_i^2}\frac{\partial W}{\partial I_2}\right), \quad (i = 1, 2). \tag{6}$$

By substituting equations eqn (1) and (2), the T_1, T_2 is

$$\begin{aligned} T_1 &= 2h_0C_1\left(\frac{\lambda_1}{\lambda_2}-\frac{1}{\lambda_1^3\lambda_2^3}\right)\left(1+\frac{C_2}{C_1}\lambda_2^2\right), \\ T_2 &= 2h_0C_1\left(\frac{\lambda_2}{\lambda_1}-\frac{1}{\lambda_1^3\lambda_2^3}\right)\left(1+\frac{C_2}{C_1}\lambda_1^2\right), \end{aligned} \tag{7}$$

where h_0 is the membrane thickness. The principal curvature k_1 and k_2 is determined by:

$$\begin{aligned} k_1 &= \frac{(\rho'\eta''-\eta'\rho'')}{(\rho'^2+\eta'^2)^{3/2}}, \\ k_2 &= \frac{-\eta'}{\rho(\rho'^2+\eta'^2)^{1/2}}. \end{aligned} \tag{8}$$

In the inflation region of the membrane, the variable ω is defined as $\omega = \frac{\mathrm{d}\lambda_2 x}{\mathrm{d}x}$. By substituting equations eqn (4), (7) and (8) into eqn (5), it is possible to obtain the equation set (λ_1,λ_2,ω), which are:

$$\begin{aligned} \lambda_1' &= -\frac{\omega-\lambda_2}{x}\frac{f_2}{f_1}-\frac{\omega}{\lambda_2 x}\frac{T_1-T_2}{f_1}, \\ \lambda_2' &= \frac{\omega-\lambda_2}{x}, \\ \omega' &= -\frac{P\lambda_1(1+e(x)^2)^{1/2}(\lambda_1^2(1+e(x)^2)-\omega^2)^{1/2}}{T_1}. \\ &\quad -\frac{\lambda_1^2(1+e(x)^2)-\omega^2T_2}{\lambda_2 x}\frac{}{T_1}+\frac{\omega(\lambda_1\lambda_1'(1+e(x)^2)+\lambda_1 e(x)e(x)')}{\lambda_1^2(1+e(x)^2)} \\ f_1 &= \frac{\partial T_1}{\partial\lambda_1};f_2=\frac{\partial T_1}{\partial\lambda_2}. \end{aligned} \tag{9}$$

The above governing system of equations applies to the inflation region in both its inflated state ($0 < x < a_0$) and compressed state ($0 < x < x_\Gamma$). The height of the inflation ellipsoid membrane is:

$$\hat{\eta} = \int_0^{a_0}(\lambda_1^2(1+e(x)^2)-\rho'^2))^{1/2}\,\mathrm{d}x. \tag{10}$$

The volumes within the membrane in the inflated state is:

$$V_{\mathrm{inf}} = 2\pi\int_0^{\hat{\eta}}\rho^2\,\mathrm{d}\eta. \tag{11}$$

3.1.3 Contact region. In a compressed state, the rigid plate flattens the ellipsoid membrane vertically and flattens where it is in contact with the membrane. Hence, the geometry of a flat membrane in the contact region ($0 < x < x_\Gamma$) is described by:

$$\eta' = 0,\ (x < x_\Gamma). \tag{12}$$

Therefore, the principal stretch in the contact region is

$$\begin{aligned} \lambda_1 &= \frac{\rho'(x)}{(1+e(x)^2)^{1/2}}, \\ \lambda_2 &= \frac{\rho(x)}{x}, \end{aligned} \tag{13}$$

assuming no friction between the contact surface of the rigid plate and the membrane. Substituting eqn (7), (8) and (13) into eqn (5), the system of equations (λ_1,λ_2,ω) governing in the contact region is:

$$\begin{aligned} \lambda_1' &= -\frac{\omega-\lambda_2}{x}\frac{f_2}{f_1}-\frac{\omega}{\lambda_2 x}\frac{T_1-T_2}{f_1} \\ \lambda_2' &= \frac{\omega-\lambda_2}{x} \\ \omega' &= \lambda_1' \\ f_1 &= \frac{\partial T_1}{\partial\lambda_1};f_2=\frac{\partial T_1}{\partial\lambda_2}. \end{aligned} \tag{14}$$

In response to compression, the reaction force on the contact area is calculated by:

$$F_c = A_cP_c = \pi x_\Gamma{}^2P_c, \tag{15}$$

where A_c is the contact area and P_c is the hydrostatic pressure in the compressed membrane. The height of the compressed ellipsoid membrane is:

$$\bar{\eta} = \int_{x_\Gamma}^{a_0}(\lambda_1^2(1+e(x)^2)-\rho'^2)^{1/2}\,\mathrm{d}x. \tag{16}$$

Hence, the volumes within the compressed state are equal as:

$$V_{\mathrm{com}} = 2\pi\int_0^{\bar{\eta}}\rho^2\,\mathrm{d}\eta. \tag{17}$$

3.1.4 Boundary conditions. The boundary conditions for the inflated state are:

$$\begin{aligned} x &= 0 \quad \lambda_1=\lambda_2=\lambda_0=\omega \\ x &= a_0 \quad \omega = 0 \end{aligned} \tag{18}$$

The boundary conditions for the compressed state are:

$$\begin{aligned} x &= 0 \quad \lambda_1=\lambda_2=\lambda_0 \\ x &= x_\Gamma \quad \lambda_{1(\mathrm{contactregion})}=\lambda_{1(\mathrm{inflationregion})} \\ x &= x_\Gamma \quad \lambda_{2(\mathrm{contactregion})}=\lambda_{2(\mathrm{inflationregion})} \\ x &= x_\Gamma \quad \omega=\lambda_1' \\ x &= a_0 \quad \lambda_{2(\mathrm{inflation})}=\lambda_{2(\mathrm{compressed})} \end{aligned} \tag{19}$$

3.1.5 Numerical solution procedure. Inflation and compression of the membrane are required. Firstly, an ellipsoid membrane is inflated to the desired shape with an inflated height $\hat{H}_{\mathrm{inf}} = \hat{\eta} - b_0$. The inflated membrane can then be compressed, with a maximum indentation depth of $\bar{H}_{\mathrm{max}} = \hat{H}_{\mathrm{inf}}$.

- Inflation: the membrane is first inflated with pressure P_0 to the desired dimension with initial conditions $\lambda_1 = \lambda_2 = \lambda_i = \omega$ at the pole of the ellipsoid membrane ($x = 0$). The bisection method is applied to find the initial values λ_i that satisfy the condition $\omega = 0$ at $x = a_0$ and record $\lambda_{2(\mathrm{inflation})}$. This condition shows that the membrane is still an ellipse shape with a perpendicular tangent at $x = a_0$. Once the dimension and shape of the ellipsoid membrane are determined, the volume of the inflated membrane V_{inf} is calculated using eqn (11).
- Compression: the second step requires assuming a liquid pressure P_c and contact point x_Γ for the compressed ellipsoid.

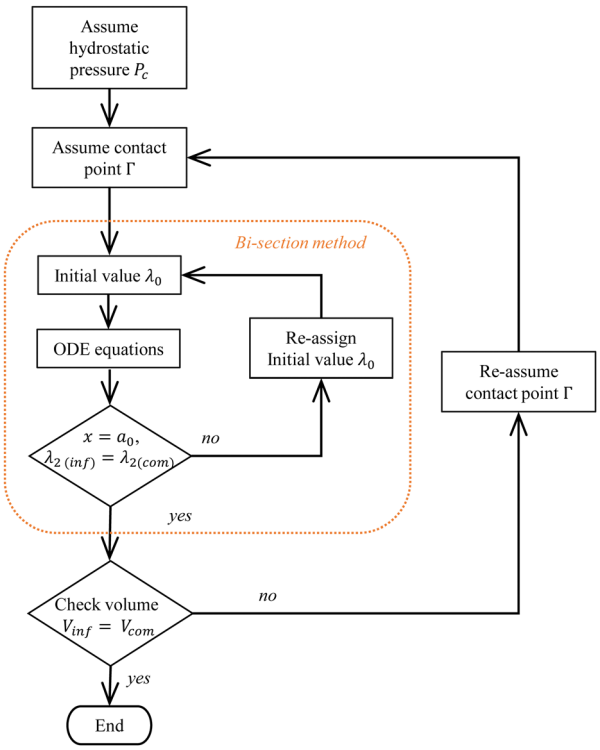

Fig. 2 Flow chart of compressed state calculations.

According to the initial condition $\lambda_1 = \lambda_2 = \lambda_0$, apply the bisection method to find the λ_0 that satisfies the second boundary conditions as shown in Fig. 2, which is the $\lambda_{2(\text{inflation})} = \lambda_{2(\text{contact})}$ at $x = a_0$. The volume of the compressed ellipsoid V_{com} is then calculated by eqn (17) to check if the volume is equal to the inflated volume V_{inf}. If it is not equal, re-assume a contact boundary x_Γ then repeat the previous calculation until the results satisfy all the restrictions and conditions shown in eqn (19).

Both steps are solved using the Runge Kutta method in Matlab 2021 with a tolerance of 10^{-2}%; the solution is usually obtained in less than 20 iterations.

3.2 Feedback actuator model

The round membrane on the feedback actuator has diameter $\varnothing d_f$; it is flat and elastic with thickness h_0. The membrane is pressurised with P_c from the ellipsoid compression. Fig. 3 shows the configuration for membrane pressurisation. The elastic material of the membrane is incompressible, resulting in a Poisson's ratio (ν) of 0.5 and causing the deformation on top (the blue area in Fig. 3) to expand evenly on the side (the red area in Fig. 3) to keep the total volume at the same level. Assuming the contact between the membrane and rigid surface is frictionless, there are no shear forces on the membrane during the pressurisation. The Young's modulus E is defined as $E = 6(1 + \alpha)C_1$ as related by the Mooney–Rivlin model. The increased diameter of the contact area is:

$$\bar{d}_f = \frac{d_f}{1 - \frac{P_c}{E}}. \tag{20}$$

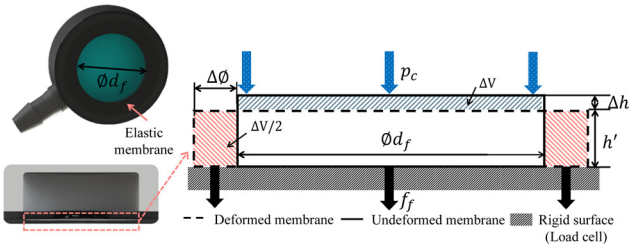

Fig. 3 The two-dimensional configuration of a pressurised flat elastic membrane on the feedback actuator. The solid line represents the undeformed membrane and the dotted line is the deformed shape of the membrane. The red and blue patterned solid is the volume change of the deformation volume during pressurisation.

With the increased diameter $\varnothing \bar{d}_f$ in the contact area, the force output under the membrane is the function of df, P_c and E defined as:

$$F_f = P_c A_f = \frac{P_c \pi}{4}\left(\frac{d_f}{1 - \frac{P_c}{E}}\right)^2, \tag{21}$$

where A_f is the contact area of the flat membrane on the feedback actuator.

4 Experiments: characterisation of the haptic feedback system

4.1 Introduction of the haptic feedback system

In our previous study, a purely hydraulic driven haptic feedback system was created with a polyjet 3D printer (Stratasys Objet500 Connex3).[7] On the one hand, a soft elastic membrane shapes the outer surface of a rigid fingertip with an inner cavity. In this paper, the fingertip sensor is approximated by an ellipsoid membrane of 1 mm thickness inspired by the average size of a human index fingertip.[34] The authors analysed the geometric dimensions of the index fingertip of 20 adults resulting in the measurements of 14 mm in height and 17 mm in width. On the other hand, a second elastic membrane is used for the base of the feedback actuator. A rigid housing with a cylindrical cavity is affixed on top of the elastic membrane. Water is used as the fluid medium inside the two cavities as well as the connecting hose. When forces are applied to the fingertip sensor, fluidic pressure inside the system acts on the membrane of the feedback actuator resulting in mechano-tactile sensation.

4.2 Experimental protocol

This experiment was carried out to verify the results from the analytical model, which demonstrates the relationship between pressure, indentation and reaction force. The ellipsoid membrane was indented 3 mm at a perpendicular direction at a speed of 0.1 mm s^{-1}, to minimised the effect of hysteresis. Related data of loading test, including pressure, indentation, the reaction force on the ellipsoid membrane and the force at the feedback actuator, is recorded by hardware sensors. Each

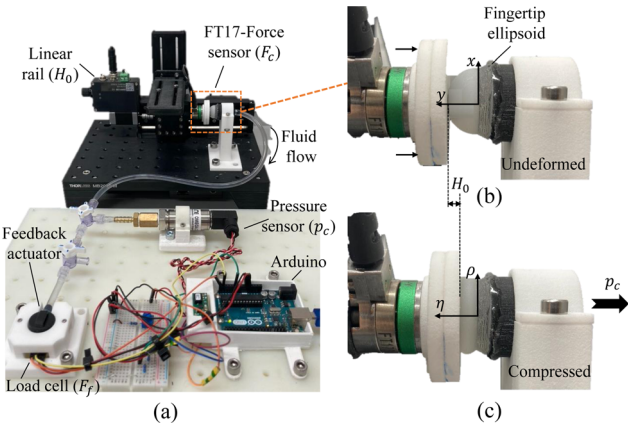

Fig. 4 Experimental setup: as shown in (a), the hydraulic haptic feedback system is mounted on a workbench. The ellipsoid fingertip membrane opposes a FT17-Force sensor, which is fixed to a linear rail. The force sensor is able to record readings during fingertip sensor indentations. The fingertip sensor is connected to the feedback actuator *via* PVC pipe. An additional load cell measures the force from the feedback actuator. A pressure transducer connected to the PVC pipe monitors hydrostatic pressure change. (b) Enlarged view of the finger ellipsoid membrane with the force sensor and indentor and (c) compressed state of ellipsoid membrane with indentation H_0 and reaction force F_c.

trial was repeated five times, and the average across the trials was reported.

4.3 Experimental setup

The experimental workbench was constructed as shown in Fig. 4. The setup consists of a liner rail (Zaber X LSM100A) with 0.05 mm sensitivity, a 3-axis force sensor (IIT FT17) with 0.318 mN sensitivity, a pressure sensor (OMEGA PXM 319001G) with 0.05 kPa sensitivity and a load cell (Honeywell FSA XX001RC4C5) with 0.22 mN sensitivity. The liner rail controls the indentation depth H_0, and the fixed force sensor records the reaction force F_c on the ellipsoid membrane. The pressure transducer records the hydrostatic pressure P_c change during the test. The feedback actuator was fixed into the socket, and the elastic membrane was in contact with the load cell to measure the blocked force F_f from the feedback actuator. The elastic finger ellipsoid and elastic membrane in feedback actuator is made from Agilus30 by a polyjet 3D printer (Stratasys Objet500 Connex3) with 0.1 mm accuracy. The hyperelastic property of Agilus30 is determined by the strain–stress curve, and the constant of Mooney–Rivlin model is C_1 = 160 355 Pa and C_2 = 46 559 Pa.[38] The entire system was immersed into water completely including the pipe and degassed by a vacuum pump to remove the air bubble inside of the closed cavity.

5 Results and discussion

5.1 Experimental and computational results

Fig. 5(a) and (b) illustrate the reaction force F_c *versus* indentation H_0 and the hydrostatic pressure P_c *versus* H_0, respectively. Both F_c and P_c show an identical non-linear increasing behaviour. The reaction force F_c is sensitive with lower indentation depth, which from 0 N to 1.6 N accounts for 50% of total indentation (0 mm to 1.5 mm). After 1.5 mm, the compression force F_c and hydrostatic pressure P_c rises non-linearly with further compression. The stiffness of the membrane shows non-linear increasing behaviour in response, as the same indentation step causes a larger increase in F_c and P_c. For an indentation smaller than 2.4 mm, the results from the model lay within the mean standard error (MSE) of the experimental data; the MSE is 0.92 for F_c, 0.584 for P_c and 0.052 for A_c. Meanwhile, increasing the initial stretch λ_0 results in the membrane stiffening at all indentation levels, especially after 1.2 mm where the deviation from the linear relationship behaves in a non-linear manner (Fig. 5(a)). If the initial stretch λ_0 is assumed to be 2.3, the model results fit best to the average of the experimental data at all indentation levels.

The contact area is a flat surface on top of the membrane that reflects the configuration of deformation in the compression stage. The contact area A_c calculated using F_c and P_c, *i.e.* ($A_c = F_c/P_c$). Fig. 5(c) shows that A_c increases rapidly at the initial compression stage, with 60% of the total contact area achieved at 4–5 N.

Fig. 6(a) shows the shape change of the membrane in the inflation stage based on the results from the model. At the initial inflation stage, the height rapidly increases, which in turn increases the aspect ratio ($\tau = b_0/a_0$) as shown in Fig. 6(a). After the initial shape change, the entire membrane expands evenly by applying a higher pressure level with a larger initial stretch ratio λ_0. Fig. 6(b) and (c) illustrate the stress resultant T_i and the stretch ratio λ_i *versus* the horizontal position x. Inflation leads to nonuniform distribution of stress and strain. The maximum stress resultant T_1 and stretch ratio λ_1 in the circumferential direction occurs at the pole of the ellipsoid membrane ($x = 0$) and decreases towards the edge of the membrane ($x = a_0$). The stress resultant and the stretch ratio in the meridian direction demonstrate an opposite behaviour compared to the circumferential direction. The transition from initial inflation to entire expansion depends on the material property and aspect ratio. In order to inflate the ellipsoid membrane from a_0 = 4.5 mm,τ = 0.6 to ρ = 9 mm with τ = 0.78. In this instance, it happens at λ_0 = 2.3 and P_i = 2.1 kPa with Agilus30. The inflation determines the lower bound of pressure in compression.

Under compression, the membrane is flattened on the top by a rigid plate while the free inflation region bulges around the membrane to keep the inside volume constant as shown in Fig. 7(a). Further compression results in higher hydrostatic pressure. Meanwhile, the stress resultant and the stretch ratio in the meridian and circumferential direction increase at all levels in response.

The points encircled with red in Fig. 7(b) and (c) are the contact boundary $\tilde{x}_\Gamma$, where $\tilde{x}_\Gamma = x_\Gamma/a_0$. From $x = 0$ to $x = x_\Gamma$, the stretch ratio (λ_1,λ_2) and the stress resultant (T_1,T_2) remains similar to their initial values but briefly decrease. In the free inflation region ($x_\Gamma < x < a_0$), the stretch ratio and the stress resultant change their behaviour by increasing in the meridian

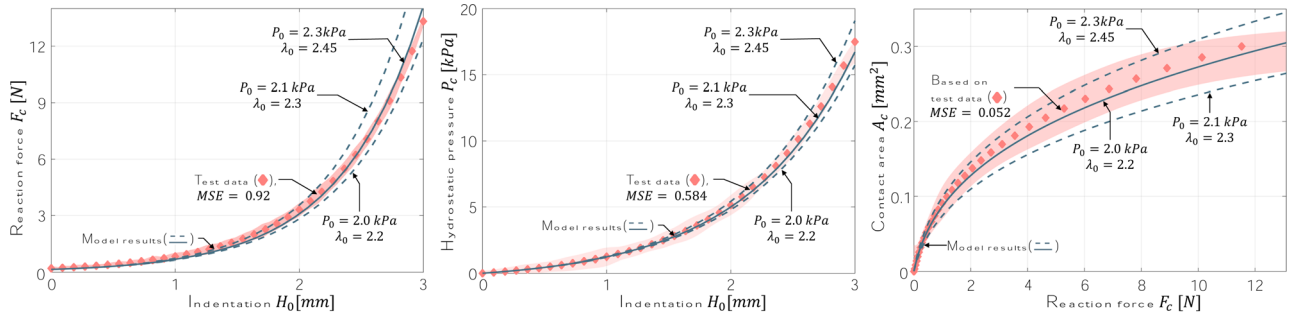

Fig. 5 Comparison between the model results and the experimental data. (a) Reaction force F_c on the membrane *versus* indentation H_0. Reaction force F_c from the model was calculated by eqn (21) (b) hydrostatic pressure P_c *versus* indentation H_0. Hydrostatic pressure P_c in the model was assumed during the calculation of eqn (9) to meet boundary conditions. (c) Contact area A_c *versus* reaction force F_c on the membrane. Contact area A_c from the model is calculated by $A_c = \pi x_\Gamma^2$.

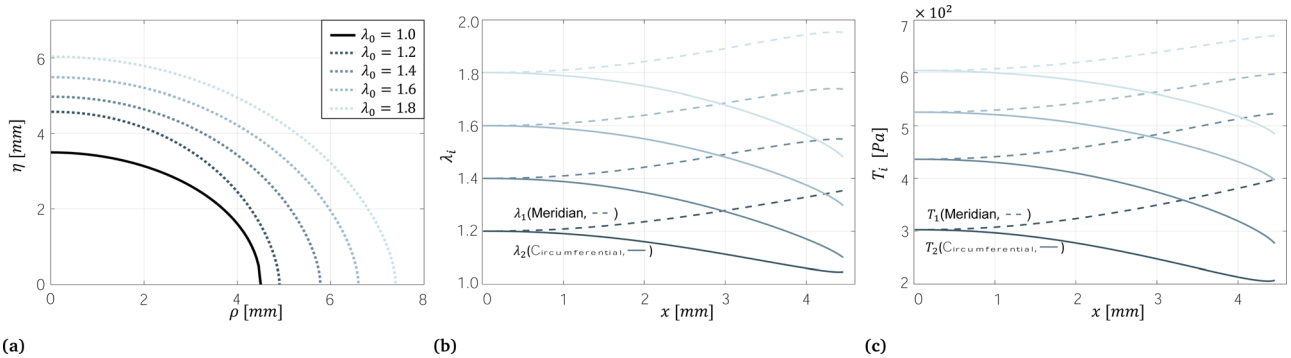

Fig. 6 Inflated membrane. At the initial inflation stage, the height increases rapidly, causing the aspect ratio τ to likewise increases. With higher pressure inflation, the entire membrane inflates evenly. (a) Cross-section view of the inflated membranes with different initial stretch ratios λ_0 calculated by eqn (10). (b) Principle stretch ratios λ_1 and λ_2 of an ellipsoid membrane calculated by eqn (9). (c) Resultant stress in the circumferential and meridian directions calculated by eqn (7).

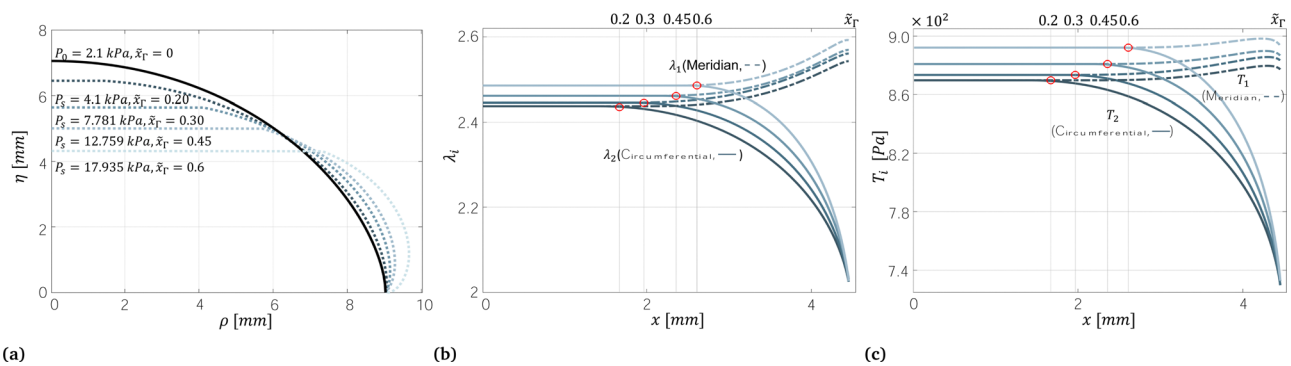

Fig. 7 Compressed membrane. With higher indentation, the membrane is flattened on the top and inflated on the side. (a) Profiles of compressed membranes with different indentation and pressure. The position of the membrane is calculated by eqn (16). (b) Principle stretch ratios λ_1 and λ_2 of an ellipsoid membrane calculated by eqn (14). (c) Resultant stress in the circumferential and meridian direction calculated by eqn (7).

direction and decreasing in the circumferential direction. In this instance, the edge of the ellipsoid membrane is constrained by satisfying $\lambda_{2(\text{inflation})} = \lambda_{2(\text{compressed})} = 2$ at $(x = a_0)$.

After verifying the analytical model of an ellipse compression, the valve is open and forms a closed cavity with the ellipsoid membrane and feedback actuator. Increased hydrostatic pressure can transmit to the ∅9 mm membrane of the feedback actuator and pressurise the membrane to generate the blocked force. The hydrostatic pressure P_c and force from the feedback actuator F_f show a linear relationship in the

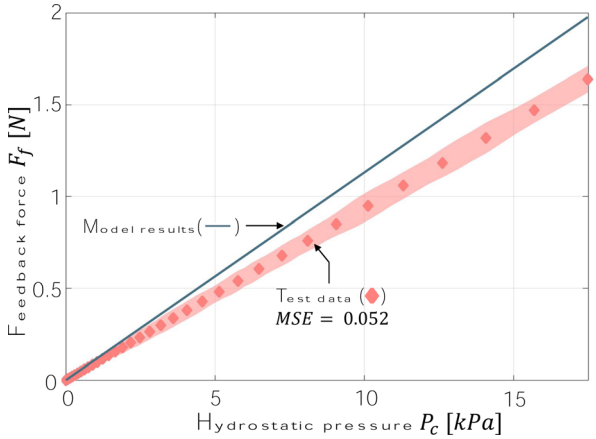

Fig. 8 Linear relationships between the output force (calculated by eqn (21)) at the feedback actuator and the hydrostatic pressure for each feedback actuator membrane.

experimental data and model results (Fig. 8). Overall, the model results show a higher force response than the experimental data; the model result reach a maximum force of 1.98 N at pressure 17.9 kPa while feedback force in the experimental data is 1.68 N at same pressure.

5.2 Discussion

As we assumed that the undeformed status in the experimental condition is equivalent to the inflated membrane in the analytical model, which is different to the experimental setup with no inflation (hence, the stress on the membrane is zero before compression), the initial inflation pressure P_0 has been considered in the compressed pressure P_c to compensate for the pressure difference in the pre-compression condition between the model and experiment. Our modelling results with minimum inflation pressure P_0 should be identical to the experimental condition, which has no inflation at the beginning (see Fig. 5). However, the force and pressure curve is lower than the experimental results (P_0 = 2.0 kPa, λ_0 = 2.2). This might be due to the negligible friction between the membrane and rigid plate. The membrane stiffens with a higher inflation pressure P_0 and stretch ratio λ_0, which results in a higher reaction force and pressure at the same indentation depth. By stiffening the membrane, it compensates for the friction disturbance and the difference between the ideal and practical conditions. In fact, the force and pressure curve shows a good agreement with the experimental results (P_0 = 2.1 kPa, λ_0 = 2.3).

After the membrane is inflated to the desired shape, the volume and the edge of the membrane is constrained by converging $\lambda_{2(\text{inflation})} = \lambda_{2(\text{contact})}$ at $x = a_0$ as it can be seen in Fig. 7(a) and (b). Within the contact region $x \in (0, x_I)$, the stretch of the membrane is isotropic, *i.e.* $\|\lambda_1 - \lambda_2\| < 10^{-2}$. As the membrane is compressed further and the contact region increases, the zone of isotropic stretching likewise increases. Where $x \in (x_I, a_0)$, the stretch in the meridian and circumferential directions are anisotropic. Meridian stress on the symmetry plane constrains the indention depth of the membrane. Moreover, circumferential stress constrains the expansion of the membrane in the vertical view.

As the indentation depth H_0 increases close to $\bar{H}_{\max}$, the initial stretch ratio λ_0 gradually increases. The stress resultant T_i likewise increases with each compression step as it is evident from (Fig. 7(b) and (c)). The membrane resists further compression by acting with higher stiffness of the material on all membranes with a higher stretch ratio and stress. The maximum indentation depth $\bar{H}_{\max}$ is determined by the inflated height $\hat{H}_{\inf}$ and original height b_0, which means the inflation stage provides the lower bound of the indentation.

During the inflation stage, slight pressure might lead to a significant expansion in the geometry due to lack of constraints at the edge of the membrane for the initial inflation. The initial dimension of the ellipsoid membrane a_0 and b_0 with the inflation condition P_0 and λ_0 are varied and have different combinations of values but can yield the same desired dimension. As a_0 and b_0 decrease with increasing inflation pressure P_0, $\hat{H}_{\inf}$ increases as well as the maximum indentation depth $\bar{H}_{\max}$ evident by a good agreement with the experiment data in Fig. 5 at higher inflation pressure values P_0. Hence, the combination with a slightly larger inflation height $\hat{H}_{\inf}$ at higher inflation pressure P_0 has been selected and compared with the indentation depth $\bar{H}_{\max}$. The initial inflation produces a nonuniform stretch and stress on the membrane as shown in Fig. 6(b) and (c). As the inflation pressure increases, the deviation level of stress and stretch ratio in the meridian and circumferential direction increases. Hence, the ellipsoid membrane shows anisotropy in the inflated states.

It is worth noting that we established a number of assumptions for our analytical model. In particular, the assumptions, that the model considers the compression of a pre-inflated membrane and that the thickness of the membrane remains unchanged, might add errors to our modelling formulation. In our paper, the membrane of the fingertip shows an anisotropic behaviour in its inflated state. In the experiments, however, the membrane is unstretched. When the inflated membrane is compressed in the computational model, the offset of the stress caused by the initial inflation remains. Hence, the results might show higher stress levels compared to the experimental results. On the other side, the change of thickness during the deformation is neglected because the thickness of the membrane is significantly smaller than the width and height of the fingertip membrane. A limitation might occur if membranes are considered that have larger thicknesses.

During the experimental procedure, the feedback actuator is mounted on a socket. The deflated membrane is then in full contact with the load cell restricting free inflation and generating blocked forces. The membrane exhibits a change in volume. Volume change ΔV (Fig. 3) can be calculated by $\Delta V = d_f \Delta h$. Under 17.935 kPa, the volume change ΔV is 1.38 mm^3, which means the total volume change of the flat membrane being pressurised by P_c is 0.432% of the volume of the inflated membrane $V_{\inf}$. Hence, the volume change of the ellipsoid membrane, in which the fluid flows to the feedback actuator, is negligible.

Table 1 Comparison between our analytical model (considering the material parameters of the human skin and Agilus30) with results from the literature showing the reaction force F_c *vs.* indentation H_0 of an ellipsoid membrane

	0.5 mm	2 mm	ε_{max}[a]
Exp. results of fingertip compression[39]	0.32 N	1.94 N	—
FEA results[36]	0.36 N	2.09 N	19.3%(0.5 mm)
Analytical (Skin)	0.27 N	1.99 N	14.7%(0.5 mm)
Analytical (Agilus30)	0.38 N	2.11 N	18.7%(0.5 mm)

[a] ε_{max}: maximum deviation error compared with experimental results from the fingertip compression.

The maximum deviation between the experimental and computational results for the feedback actuator is about 18.56% at a pressure value of 17.9 kPa in Fig. 8. It can be observed that the deviation proportionally increases with the hydrostatic pressure. The reasons for this discrepancy might be manifold. One reason might be due to the increase in friction between the surface of the elastic membrane and the load cell preventing the membrane to stretch. This behaviour is neglected in our computational model of the feedback actuator. Another reason might relate to the manufacturing process of the actuator. The membrane is fixed onto the solid structure by the multi-material 3D printer by Stratasys. The bond between these two materials might vary in strength.

The computational results of our analytical model are compared to results reported in the literature as summarised in Table 1. The table shows the calculated or measured reaction force F_c at H_0 = 0.5 mm and 2 mm indentation. As a reference, the experimental results of force-indentation of a fingertip were reported by Serina.[39] Then, the computational results of an FEA[36] are listed in the table as well as the results of our model using the material constants of skin tissue (C_1 = 13 400 Pa, C_2 = 29 500 Pa)[34] on the one hand and the material contestants of Aglius30 on the other hand. Maximum errors are calculated with respect to the experimental results of a fingertip compression. When considering the constants of Aglius30 material, the maximum error is similar to the results of the FEA. The error is lower (14.7%) for results taking the material constants of human skin tissue as input.

6 Conclusions

This paper derived and validated an analytical compression model for both an ellipsoid and a flat membrane as well as validated the models based on experimental data. The model is capable to capture the ellipsoid membrane's non-linear force response under compression in line with experimental data (Fig. 5). In our approach, we used the Cartesian coordinate to obtain the ODE equations, which differs from the use of a polar coordinate by ref. 34 resulting in a simplified set of ODEs. By inserting the dimension of the ellipsoid membrane (a_0,b_0), material property (C_1,C_2) and thickness (h_0), the inflation and compression can be solved, considering the hydrostatic pressure P_c, reaction force F_c and contact area A_c with membrane shape deformation as illustrated in Fig. 5. In our case study, the elastic ellipsoid membrane has a major axis length of 9 mm with a minor axis length of 7 mm similar to the average size of a natural human fingertip producing similar non-linear force-indentation relationship of the human fingertip with a semblable force level of 0–4 N at 0–2 mm indentation.[39]

Our theoretical computations can predict the inflated and compressed states of the ellipsoid membrane. Hence, by designing the haptic feedback system for different sizes of fingertip membranes and feedback actuators with different elastic materials, the model can predict the performance of the haptic feedback system and optimise the design to replicate the force-indentation curve. The deformation theory for the ellipsoid membrane is not only limited to modelling the fingertip compression but also has the potential to model inflation and compression of an ellipsoid membrane in generic cases.

Author contributions

Ge Shi: Methodology, software, hardware setup, formal analysis, investigation, data curation, writing – original draft, visualization. Azadeh Shariati: investigation, writing – review & editing. Ian Eames: methodology, software, formal analysis, writing – review & editing. Helge A. Wurdemann: conceptualization, methodology, resources, supervision, writing – review & editing, visualization, project administration, funding acquisition.

Conflicts of interest

There are no conflicts to declare.

Acknowledgements

This research has been supported by the Grand Challenges Small Grant received from UCL Grand Challenges, the Engineering and Physical Sciences Research Council (grant number: EP/V01062X/1) and UCL-IIT Delhi Seed Funding 2020-21 received from UCL Global Engagement.

Notes and references

1 J. S. Schofield, K. R. Evans, J. P. Carey and J. S. Hebert, Applications of sensory feedback in motorized upper extremity prosthesis: a review, *Expert Rev. Med. Devices*, 2014, **11**, 499–511.
2 P. Svensson, U. Wijk, A. Björkman and C. Antfolk, A review of invasive and non-invasive sensory feedback in upper limb prostheses, *Expert Rev. Med. Devices*, 2017, **14**, 439–447.
3 D. S. Childress, Closed-loop control in prosthetic systems: historical perspective, *Ann. Biomed. Eng.*, 1980, **8**, 293–303.
4 J. J. E. Conzelman, H. B. Ellis and C. W. O'brien, *Prosthetic device sensory attachment*, *US Pat.*, 2656545, 1953.

5 C. Antfolk, A. Björkman, S.-O. Frank, F. Sebelius, G. Lundborg and B. Rosen, Sensory feedback from a prosthetic hand based on air-mediated pressure from the hand to the forearm skin, *J. Rehabilitation Med.*, 2012, **44**, 702–707.
6 M. F. Simons, K. M. Digumarti, N. H. Le, H.-Y. Chen, S. C. Carreira, N. S. Zaghloul, R. S. Diteesawat, M. Garrad, A. T. Conn and C. Kent, *et al.*, B: ionic glove: a soft smart wearable sensory feedback device for upper limb robotic prostheses, *IEEE Rob. Automation Lett.*, 2021, **6**, 3311–3316.
7 G. Shi, A. Palombi, Z. Lim, A. Astolfi, A. Burani, S. Campagnini, F. G. Loizzo, M. L. Preti, A. M. Vargas and E. Peperoni, *et al.*, Fluidic haptic interface for mechano-tactile feedback, *IEEE Trans. Haptics*, 2020, **13**, 204–210.
8 B. A. Trimmer, New challenges in biorobotics: incorporating soft tissue into control systems, *Appl. Bionics and Biomechanics*, 2008, **5**, 119–126.
9 N. Herzig, J. Jones, E. Perez-Guagnelli and D. D. Damian, *Model and validation of a highly extensible and tough actuator based on a ballooning membrane, 2021 IEEE International Conference on Robotics and Automation (ICRA)*, 2021, 11961–11967.
10 J. Barreiros, I. Karakurt, P. Agarwal, T. Agcayazi, S. Reese, K. Healy and Y. Menguc, *Self-sensing Elastomeric Membrane for Haptic Bubble Arrray., 2020 3rd IEEE International Conference on Soft Robotics (RoboSoft)*, 229–236.
11 S. Sareh, A. Jiang, A. Faragasso, Y. Noh, T. Nanayakkara, P. Dasgupta, L. D. Seneviratne, H. A. Wurdemann and K. Althoefer, *Bio-inspired tactile sensor sleeve for surgical soft manipulators, 2014 IEEE International Conference on Robotics and Automation (ICRA)*, 1454–1459.
12 H. A. Sonar, A. P. Gerratt, S. P. Lacour and J. Paik, Closed-loop haptic feedback control using a self-sensing soft pneumatic actuator skin, *Soft Robot.*, 2020, **7**, 22–29.
13 F. Veiga, B. Edin and J. Peters, Grip stabilization through independent finger tactile feedback control, *Sensors*, 2020, **20**, 1748.
14 O. S. Osman, J. L. Selway, M. A. Kepczyńska, C. J. Stocker, J. F. O'Dowd, M. A. Cawthorne, J. R. Arch, S. Jassim and K. Langlands, A novel automated image analysis method for accurate adipocyte quantification, *Adipocyte*, 2013, **2**, 160–164.
15 D. R. Grimes and F. J. Currell, Oxygen diffusion in ellipsoidal tumour spheroids, *J. R. Soc., Interface*, 2018, **15**, 20180256.
16 A. Stanzione, A. Ponsiglione, G. A. Di Fiore, S. G. Picchi, M. Di Stasi, F. Verde, M. Petretta, M. Imbriaco and R. Cuocolo, Prostate volume estimation on MRI: accuracy and effects of ellipsoid and bullet-shaped measurements on PSA density, *Acad. Radiol.*, 2021, **28**, e219–e226.
17 C. Pozrikidis, *Modeling and simulation of capsules and biological cells*, Chapman and Hall/CRC, 2003.
18 M. W. Keller and N. R. Sottos, Mechanical properties of microcapsules used in a self-healing polymer, *Exp. Mech.*, 2006, **46**, 725–733.
19 W.-H. Hsu, Y.-H. Chien and H.-Y. Tsai, Experimental and Modeling Analysis of the Cell-Wall Fracture of Nannochloropsis Oculata, *J. Mech.*, 2020, **36**, 789–797.
20 C. L. Eccles, R. Patel, A. K. Simeonov, G. Lockwood, M. Haider and L. A. Dawson, Comparison of liver tumor motion with and without abdominal compression using cine-magnetic resonance imaging, *Int. J. Radiat. Oncol., Biol., Phys.*, 2011, **79**, 602–608.
21 M. Mooney, A theory of large elastic deformation, *J. Appl. Phys.*, 1940, **11**, 582–592.
22 R. S. Rivlin, Large elastic deformations of isotropic materials IV. Further developments of the general theory, *Philos. Trans. R. Soc., A*, 1948, **241**, 379–397.
23 J. E. Adkins and R. S. Rivlin, Large elastic deformations of isotropic materials IX. The deformation of thin shells, *Philos. Trans. R. Soc., A*, 1952, **244**, 505–531.
24 W. Yang and W. Feng, On axisymmetrical deformations of nonlinear membranes, *J. Appl. Mech.*, 1970, **37**, 1002–1011.
25 W. Feng and P. Huang, On the inflation of a plane nonlinear membrane, *J. Appl. Mech.*, 1974, **41**, 767–771.
26 Y. Bouremel, I. Eames, S. Madaan, S. Brocchini and P. T. Khaw, Compression of pressurised elastic pockets, *Int. J. Non Linear Mech.*, 2018, **107**, 10–15.
27 W. Feng and W.-H. Yang, On the contact problem of an inflated spherical nonlinear membrane, *J. Appl. Mech.*, 1973, **40**, 209–214.
28 G. Sun and Z. Zhang, Mechanical strength of microcapsules made of different wall materials, *Int. J. Pharm.*, 2002, **242**, 307–311.
29 S. Mettu, Q. Ye, M. Zhou, R. Dagastine and M. Ashokkumar, Ultrasonically synthesized organic liquid-filled chitosan microcapsules: part 2: characterization using AFM (atomic force microscopy) and combined AFM-confocal laser scanning fluorescence microscopy, *Soft Matter*, 2018, **14**, 3192–3201.
30 D. Margolis, J. Tylee and D. Hrovat, Heave mode dynamics of a tracked air cushion vehicle with semiactive airbag secondary suspension, *J. Dyn. Syst., Meas., Control*, 1975, **97**, 399–407.
31 X. Yang, L. Yu and R. Long, Contact mechanics of inflated circular membrane under large deformation: analytical solutions, *Int. J. Solids Struct.*, 2021, **233**, 111222.
32 G. Tamadapu and A. DasGupta, Finite inflation analysis of a hyperelastic toroidal membrane of initially circular cross-section, *Int. J. Non Linear Mech.*, 2013, **49**, 31–39.
33 X. Li and D. Steigmann, Finite deformation of a pressurized toroidal membrane, *Int. J. Non Linear Mech.*, 1995, **30**, 583–595.
34 E. R. Serina, E. Mockensturm, C. Mote Jr and D. Rempel, A structural model of the forced compression of the fingertip pulp, *J. Biomech.*, 1998, **31**, 639–646.
35 T. Inoue and S. Hirai, Elastic model of deformable fingertip for soft-fingered manipulation, *IEEE Trans. Robot.*, 2006, **22**, 1273–1279.
36 J. Z. Wu, R. G. Dong, S. Rakheja and A. Schopper, Simulation of mechanical responses of fingertip to dynamic loading, *Med. Eng. Phys.*, 2002, **24**, 253–264.
37 J. Z. Wu, R. G. Dong, S. Rakheja, A. Schopper and W. Smutz, A structural fingertip model for simulating of the biomechanics of tactile sensation, *Med. Eng. Phys.*, 2004, **26**, 165–175.
38 F. F. Abayazid and M. Ghajari, Material characterisation of additively manufactured elastomers at different strain rates and build orientations, *Addit. Manuf.*, 2020, **33**, 101160.
39 E. R. Serina, C. Mote Jr and D. Rempel, Force response of the fingertip pulp to repeated compression—effects of loading rate, loading angle and anthropometry, *J. Biomech.*, 1997, **30**, 1035–1040.